Self-activated healing of delamination damage in woven composites

M. R. Kessler[a] and S. R. White[b]

[a]Department of Theoretical and Applied Mechanics
[b]Department of Aeronautical and Astronautical Engineering
University of Illinois at Urbana-Champaign

Abstract

A study of the healing of delamination damage in woven E-glass/epoxy composites is performed. With the ultimate goal of *self-healing* in mind, two types of healing processes are studied. In the first a catalyzed monomer is manually injected into the delamination. In the second a *self-activated* material is created by embedding the catalyst directly into the matrix of the composite, then manually injecting the monomer. Healing efficiencies relative to the virgin fracture toughness of up to 67% are obtained when the catalyzed monomer is injected and about 21% for the self-activated materials. Scanning electron microscopy is used to analyze the fracture surfaces and provide physical evidence of repair. The healing efficiency is found to be controlled by three primary factors: (1) interfacial bond strength between the healing agent and the fiber, (2) the *in-situ* polymerization rate of the healing agent, and (3) the degree of fiber bridging.

Keywords: A. Polymer-matrix composites (PMCs); B. Delamination; B. Fracture toughness; E. Repair

1. Introduction

No matter how carefully structural materials are designed and manufactured, all will eventually fail either by a catastrophic event or through natural degradation. Recently a novel approach to the later problem was reported in *Science* [1]. The article describes a material with the ability to heal itself autonomically, i.e. a *self-healing* material. Such materials are capable of resisting and slowing down the natural degradation process, thereby prolonging their useful service life.

The self-healing concept [1] is shown in Fig. 1. A monomer healing agent is stored in microcapsules that are dispersed throughout a polymer matrix. When damage occurs, a crack propagates through the material and breaks open the microcapsules, thereby releasing the healing agent into the crack by capillary action. Once in the crack plane, the healing agent contacts an embedded catalyst triggering a ring-opening metathesis polymerization (ROMP) that effectively bonds the crack faces closed.

This paper reports on initial studies using a self-healing polymer as the matrix material of a polymeric structural composite. In particular, we report on the healing of interlaminar fracture damage in woven composites. Interlaminar fracture (delamination) often occurs in composites as a result of low energy impact or manufacturing defects. It is difficult to detect and repair because the defect is typically confined to subsurface locations. Once delaminations are present, they can grow when the structure is loaded [2]. Additionally, interlaminar fracture can initiate from regions of stress concentration such as holes or resin micro cracks and then proceed by delamination [3].

Woven composites are an ideal candidate for the use of a self-healing polymer matrix because of the architecture of the reinforcement. Large resin rich areas are formed in woven composites by the interlacing of undulating warp and fill yarns [4]. These interstitial areas serve as natural sites for storage of the microcapsules (50-100 μm diameter) used in self-healing polymers since their presence will not disrupt the inherent undulation of the fiber tows (as would occur for unidirectional fiber tows). Depending on the architecture of the weave and the fiber volume fraction, a large number of microcapsules can be stored in the interstitial regions without significantly changing the bulk material properties of the composite.

The development of a self-healing *composite* is fundamentally more difficult than the self-healing *polymer* reported in [1]. Although resin micro-cracks can be healed similarly, the presence of the fiber reinforcement increases the number of damage modes and the complexity of the healing process. In this paper we report on initial studies assessing the efficiency of the self-healing concept shown in Fig. 1 for healing interlaminar fracture damage in woven composite materials. The materials used in this

study and the experiments performed are described first, followed by a detailed discussion and presentation of the results.

2. Experimental

While achieving *in-situ* self-healing in a structural composite is our ultimate goal, we have approached the problem in a more focused and evolutionary manner. First, it must be established that the healing agent system is capable of achieving reasonable levels of repair in the composite material. This is accomplished by manually injecting catalyzed healing agent into the delamination region of a composite specimen and mechanically testing after the ROMP reaction is complete. The second step is to show that the *embedded* catalyst remains active after composite curing and is still capable of triggering the ROMP polymerization of the healing agent. In this case, uncatalyzed healing agent is manually injected into the delamination of a *self-activated* (embedded catalyst) composite sample and mechanical testing of the sample occurs after an appropriate time period. Third, it must be confirmed that the embedded microcapsules rupture during propagation of the delamination, thereby releasing the healing agent into the crack plane. Simply embedding microcapsules in a composite sample and examining the fracture surface after testing can provide this data. The final step is to combine each of these aspects into a fully integrated in-situ system.

We report on the successful completion of the first two of these aspects in this paper. Double cantilever beam (DCB) testing [5] was used to provide a means of assessing the healing efficiency of manual injection and self-activated healing. DCB testing was first introduced for the evaluation of adhesive strength [6]and has been extensively used for interlaminar fracture studies in composite materials since then [7-19]. The specimen fabrication procedure and experimental methods that were used are presented first.

2.1 Specimen Manufacture and Preparation

An epoxy matrix was formulated by mixing EPON 828 (Miller-Stephenson Chemical Co.), a bisphenol-A based epoxide, and diethylenetriamine (DETA) curing agent (Air Products and Chemicals, Inc.) at a concentration of 12:100 (by wt.) curing agent to epoxide. Both eight-harness (8H) satin weave and plain weave E-glass fabric (Fibre Glast Development Corp.) were used as reinforcement (see Table 1). For two groups of samples bis(tricyclohexylphosphine)benzylidine ruthenium (IV) dichloride (Grubbs' catalyst) was mixed with the epoxy resin at a concentration of 1.75% (wt.) and

used to impregnate the center two fabric layers. The Grubbs' catalyst was supplied by Strem Chemicals, Inc. in the form of a fine purple powder.

Dicyclopentadiene (DCPD) monomer stabilized with 100 – 200 ppm p-tert-butylcatechol (Acros Organics) was used as a healing agent. DCPD is a clear, colorless liquid with a viscosity of 0.736 centipoise at 21 °C. When DCPD mixes with Grubbs' catalyst a ring-opening metathesis polymerization (ROMP) reaction is triggered resulting in poly(DCPD), a thermosetting polymer. This ROMP reaction is rapid at room temperatures and is completed within 1-5 min. Grubbs' catalyst is highly reactive for double-bond metathesis while exhibiting exceptional tolerance to other functional groups [20].

Composite panels 300 mm x 300 mm were fabricated by hand layup and compression molded. Panels consisted of 10 or 12 plies of fabric yielding a nominal thickness of 5 mm after cure. A 13 μm thick Teflon film (Norton Perfomance Plastics) was placed at the midplane of the panel to create the initial delamination crack. Four types of double cantilever beam (DCB) specimens were made as described in Table 1. For two groups of specimens Grubbs' catalyst was embedded in the composite matrix in two locations. First, 1.75% (wt.) was mixed into the resin that was used to impregnate the center two fabric layers. Second, 50 mg (0.17% wt.) or 100 mg (0.33% wt.) per specimen of catalyst was manually dispersed in a region extending 75 mm beyond the Teflon insert along the midplane. The panels were cured at room temperature for 24 h followed by 24 h at 40 °C. The fiber volume fraction, determined by matrix digestion [21], was measured to be 27% and 29% for the plain weave and satin weave specimens, respectively.

Once the panels were cured, they were machined using a water cooled diamond saw to produce DCB specimens 25 mm wide x 140 mm long x 5 mm thick. The Teflon insert extended for approximately 64 mm along the midplane of the specimen. A pair of hinge tabs was bonded to the end of each specimen with an epoxy adhesive (Fig. 2).

2.2 Test Procedure

The specimens were tested using an Instron Model 8500+ tensile test machine in displacement control at a rate of 5 mm/min following the testing procedure of ASTM standard D 5528-94a [5]. One edge of the specimen was coated with a thin layer of white opaque fluid to aid in visualization of the crack tip. Thin vertical lines were marked every 1 mm to provide a reverence for crack length measurement. A traveling optical microscope was positioned on the side of the specimen to observe the crack tip as it propagated during the test. A CCD camera connected to the microscope was used to record optical images of the crack position throughout the test. Figure 3 shows the test set-up along with a sample image from the microscope.

4

Specimens were initially loaded until reaching 40 - 50 mm total crack opening displacement. Load and displacement were recorded throughout the test, along with optical images of the crack tip position. At the end of loading and with the crack fully open, healing agent was injected into the delamination area using a syringe. For the reference group of specimens the DCPD healing agent was catalyzed manually by mixing with 1.38% (wt.) Grubbs' catalyst before injection. For the self-activated (embedded catalyst) group of specimens, only pure DCPD was injected.

After injection of the healing agent, the specimen was unloaded and clamped closed. After a 48 h period of healing, the unmarked edge of the specimen was coated and then marked with vertical lines at 1 mm intervals. The specimen was reloaded to 40 – 50 mm total crack opening displacement and then unloaded while recording load, displacement, and crack position.

2.3 Data Reduction

The analysis of the double cantilever beam test is based on linear elastic fracture mechanics and beam mechanics. We begin by expressing the energy release rate in terms of the sample compliance for displacement control [22]

$$G = -\frac{1}{b}\left(\frac{\partial \Pi}{\partial a}\right)_\delta = \frac{1}{2b}P^2\frac{dC}{da} \qquad (1)$$

where Π is the potential energy of the specimen, b is the width, a is the crack length, P is the load, δ is the opening displacement, and C is the compliance (δ/P).

It is common to assume that each arm of the DCB specimen acts as a cantilever beam. With this assumption and using linear beam theory with eq. (1), the mode I strain energy release rate (G_I) becomes,

$$G_I = \frac{3P\delta}{2ba^*} \qquad . \qquad (2)$$

In practice eq. (2) overestimates G_I because it neglects the contributions of shear deformation and rotation that may occur at the delamination front. In effect, the compliance as calculated by linear beam theory corresponds to a specimen with a crack length of $a + \Delta$, where Δ is the contribution from shear and rotation. The effective crack length is then $a^* = a + \Delta$ where Δ is determined by plotting the cube root of the specimen compliance (δ/P) versus crack length (a) [23] as illustrated in Fig. 4. This approach to the analysis of the DCB specimen is referred to as the modified beam theory (MBT) method [5].

3. Results and discussion

3.1 Typical Load Displacement Results

Figure 5 shows a typical load displacement curve for a DCB specimen. The behavior is linear up to the onset of crack growth near the peak load of about 55 N. Upon further displacement, the crack advances along the midplane in a stable fashion and the load drops slowly. At the end of the virgin loading cycle (δ = 40 mm), a mixture of DCPD and Grubbs' catalyst was injected into the delamination with a syringe while the specimen was under load so that full access was provided to the delamination. After injection of the healing agent, the specimen was unloaded and allowed to heal for 48 hours. Upon retesting, the healed specimen closely follows the original loading curve until crack propagation begins anew near the peak load of about 40 N. Crack advancement then occurs through the *healed* region as displacement increases until the healed loading curve intersects the unloading curve of the virgin specimen (pt. D in Fig. 5). At this point, the crack has advanced through the entire healed region and further loading propagates a new "virgin" crack.

3.2 Reference Specimens

Samples in which the healing agent was manually catalyzed before injection are designated as reference specimens. The results of reference specimen testing are believed to provide an upper limit for the healing efficiency under ideal conditions and it provides a benchmark for comparison to specimens in which the catalyst is embedded in the matrix. Figure 5 shows a typical loading curve for an 8H satin fabric E-glass/epoxy reference specimen.

The typical loading curve for a plain weave E-glass/epoxy reference specimen is shown in Fig. 6. During crack propagation for the virgin loading curve there are several points where the load suddenly drops and the crack jumps ahead. This stick-slip crack growth is erratic and complex. It is referred to by Smiley and Pipes [10] as a transition between ductile stable and brittle unstable crack growth. Unstable crack propagation in brittle composites has been reported in other literature [2-4,10-13,24]. After completing the virgin loading cycle a mixture of DCPD and Grubbs' catalyst (1.38% wt.) was injected into the crack and the specimen was unloaded. Retesting after 48 hours of healing, a stable crack propagation was exhibited throughout the healed region.

As a control experiment, pure DCPD (not catalyzed) was injected into reference specimens. After waiting 48 h and then retesting, no evidence of healing could be found.

6

3.3 Self-activated Specimens

In order to assess the feasibility of achieving *in-situ* self-healing, specimens were fabricated with the catalyst embedded directly into the epoxy matrix. Healing for these specimens was accomplished by injecting pure DCPD into the delamination while the ROMP reaction self-activates by contact with the embedded catalyst.

Figure 7 shows a typical loading curve for a self-activated specimen. After injecting DCPD once the virgin loading is completed, healing commences as the DCPD monomer mixes with the embedded catalyst near or on the crack plane. Retesting after 48 hours shows a modest amount of healing for this specimen.

In Fig. 8 an example result for a plain weave specimen is shown. Here the crack growth for the virgin loading is more unstable than for the reference plain weave specimen, and a single, rapid crack propagation occurs during initial loading. Conversely, the healed loading cycle exhibits stable crack propagation throughout.

Grubbs' catalyst and DCPD initiate a *living* ring opening metathesis polymerization. The terminology here is indicative of the ability of the still-active poly(DCPD) chain ends to continuously initiate growth as more monomer is added, thereby forming a *living* polymer chain. If new monomer is supplied at any time to the end of the chain, further ROMP occurs and the chain extends.

For self-healing composites the use of a living polymerization for the healing agent system is extremely beneficial since multiple healings can be accomplished simply by replenishing the supply of the DCPD monomer. In contrast, for normal polymerization reactions, after the catalyst has triggered the initial polymerization the polymer chain ends are terminated and no further healing events are possible.

To demonstrate the ability to achieve multiple healings with Grubbs' catalyst and DCPD, a self-activated DCB specimen was tested four times in succession while injecting pure DCPD into the delamination plane each time. Figure 9 shows the results of this series of tests for a plain weave specimen. The virgin test results for this specimen are shown in Fig. 8. The peak load actually shows a slight increase with each subsequent healing event. The level of recovery of fracture toughness compared to the virgin loading is quite good in all cases - between 50-60% of the peak load.

3.4 Fracture Toughness and Repair Efficiency

In order to quantify the amount of healing that occurs in DCB specimens, it is more informative to calculate the fracture toughness rather than comparing peak load. The data reduction necessary to obtain fracture toughness is first obtained by resolving load vs. crack length from the microscope images and load frame output during the test.

An example is shown in Fig. 10. The vertical tick marks correspond to one millimeter increments in crack length from the initial value a_0 to the final value a_f.

Following the methodology presented in §2.3, the compliance of the DCB specimen is then calculated and the cube root of compliance versus crack length is plotted as in Fig. 4. A linear least squares fit to this plot shows very good correlation to the experimental data and the intersection of this curve with the x-axis yields the crack length offset Δ used in the modified beam theory. The fracture toughness is then calculated using eq. (2).

It is particularly difficult to accurately identify the fracture toughness at the initiation of crack growth unless there is a clearly defined load drop in the load-displacement curve at initiation. One method [5] of overcoming this problem is to define the "initiation" fracture toughness as the point of intersection of the experimental curve and a line drawn from the origin equal to a 5% increase in compliance (compared to the initial linear portion of the loading cycle). The result for a typical loading cycle is shown in Fig. 10. Taking the load and displacement at the intersection as P_0 and δ_o, and knowing the initial crack length a_o and the offset Δ, the initiation fracture toughness is then obtained using eq. (2). Subsequent calculations of fracture toughness are then obtained by measuring (P, δ, a) at each of the tick marks indicated in Fig. 10.

A plot of G_{IC} versus crack length shows a characteristic R-curve behavior for each group of specimens. An example is shown in Fig. 11 for the self-activated satin weave specimens. The strain energy release rate increases with crack length until it reaches a plateau value that is roughly twice that at initiation. The principal reasons for the increased resistance to delamination with crack length is the development of fiber bridging between plies and the development of the damage zone around the crack tip [16-19,25]. Fiber bridging in the specimens was confirmed by optical microscopy during DCB testing and by scanning electron microscopy (SEM) of the fracture surfaces afterwards.

As shown in Fig. 11 there is a significant amount of scatter in the data between specimens. Such behavior is characteristic of DCB testing of woven composite materials in general [13,16-18,26]. For any given specimen, the plateau value of G_{IC} tends to vary somewhat with crack length as well. Variations in G_{IC} with crack length are most likely the result of either changes in the amount of fiber bridging (perhaps as a large group of bridging fibers suddenly breaks) or in the size of the damage zone at the crack tip as the crack passes through resin rich pockets (at crossover points in the weave for example). Hereafter, the individual test results are averaged at any given crack length and the overall R-curve behavior for each group of specimens is reported using these averages.

8

In Fig. 12 the average R-curves for both reference groups (satin and plain weave specimens) are presented. Each data point represents the average fracture toughness for all specimens at that crack length.

For all reference specimens in both virgin and healed conditions, the fracture toughness steadily increases with crack length until reaching a steady state condition after about 10 mm crack extension. The plateau values are roughly twice the initiation values for the plain weave specimens, whereas the satin weave specimens show an increase of about 1.5X. Interestingly, the plateau values for the healed condition are roughly the same as the initiation values for the virgin tests. Obviously, if a crack propagates during the healed test along the original crack plane that was created during the virgin testing, then no fiber bridging can occur. At initiation for the virgin tests, there is no fiber bridging contribution to the fracture toughness.

The fact that testing of the healed specimens exhibits R-curve behavior is indicative of other contributing mechanisms to the increase in fracture toughness with crack length. In fact, the damage zone during healed testing is less constrained (by bridging fibers for example) and would be expected to contribute more strongly to increased fracture toughness.

Figure 13 shows a typical R-curve for one of the self-activated specimens corresponding to the load-displacement curve in Fig. 8. For the virgin test crack propagation occurred primarily in one large unstable jump, with the fracture toughness at the moment of crack arrest about equal to that at initiation. Because of the unstable nature of crack propagation, an average R-curve cannot be determined. By defining the plateau value of the fracture toughness as the peak value prior to unstable fracture, an average for the virgin condition was calculated to be 1052 J/m^2.

A summary of all DCB testing is given in Table 2. Average values for initiation and plateau fracture toughness are reported together with the standard deviation for each of the four groups of specimens in both virgin and healed conditions. To quantify the level of healing for each group of specimens the healing efficiency is defined as [27]

$$\eta = \frac{G_{IC}^{Healed}}{G_{IC}^{Virgin}} \qquad (4)$$

where G_{IC}^{Healed} and G_{IC}^{Virgin} refer to either the initiation or plateau values of healed and virgin conditions.

(a) Reference Specimens

The reference specimens showed the highest healing and because mixing of the catalyst is manually controlled they provide an upper bound for self-activated specimens. Although specimens with satin weave architecture showed the highest healing efficiencies, the largest plateau G_{IC}^{Healed} was achieved for the plain weave specimens.

A detailed post fracture analysis was performed on selected specimens using optical and scanning electron microscopy. Figure 14 shows a series of images at increasing magnification of the virgin fracture surface for a satin weave reference specimen. It is clear from the images that failure was dominated by interfacial debonding between fiber and matrix. Very little resin is left on the fiber bundles and at the highest magnification the fibers appear to be relatively clean. This evidence indicates that the delamination propagates preferentially between the fiber bundles of one ply and the thin layer of resin separating it from the neighboring ply, a mechanism also observed in woven glass composites by Ebling *et al.* [4]. There is also clear evidence in Fig. 14 of broken fibers, indicative of fiber bridging as the delamination propagates along the mid-plane.

Since the crack prefers to separate the fiber bundles from the surrounding matrix, the crack path follows the contour of the woven cloth. As a result, the architecture of the cloth imposes a more tortuous crack path than would be expected from the neat resin alone, or with unidirectional composites constructed of the same materials. Thus, the virgin fracture toughness is higher than EPON 828/DETA epoxy (320 J/m^2) or unidirectional E-glass/epoxy [7].

Similar features are present on the virgin fracture surface of a plain weave reference specimen as shown in Fig. 15. Again, failure is primarily by interfacial debonding and evidence of fiber bridging is apparent. One feature unique to the plain weave specimens is the large resin rich interstitial regions where the warp and fill tows crossover.

Examination of these regions in more detail is provided in Fig. 16. Three different magnifications of the same interstitial area are shown. At the lowest magnification, the location and overall features are evident relative to the neighboring fiber tows. The next higher magnification shows the fiber imprints in the matrix where fibers have debonded. There is also clear evidence of fiber bridging in which several fibers are broken at the edge of the interstitial area. At the highest magnification, a relatively clean fiber protrudes from the matrix indicating fiber debonding as the primary mode of fracture.

Scanning electron microscopy was also performed on the fracture surfaces of healed reference specimens in order to look for physical evidence of healing. In Fig. 17 a typical image of the fracture surface from a healed plain weave specimen is shown. The large region of relatively smooth appearance is the polymerized DCPD healing agent.

Verification was accomplished by physically removing some of the polymer film and performing FTIR analysis of the sample. A characteristic peak at 965 cm^{-1} was found corresponding to the trans double bond in poly(DCPD).

Having confirmed the presence of the polymerized healing agent, several features of the fracture surface are clearly evident. The fracture surface is relatively smooth and the healed fracture plane follows the same contour as the virgin fracture plane. Thus, no fiber bridging can be expected upon retesting in the healed condition. It is also apparent that the healing agent is present only on a portion of the original (virgin) fracture plane. Incomplete coverage could be the result of diffusion of the DCPD monomer into the matrix if polymerization proceeds at a slower rate than diffusion of the monomer.

Further physical evidence of the presence of the healing agent on the fracture surface is provided in Fig. 18. Here a close-up view of a region surrounding one of the fibers on the fracture surface is shown. At the highest magnification the poly(DCPD) film is shown still attached to one of the fibers. A significant amount of plastic flow of the healing agent is evident by the numerous bands and finger-like projections of the film.

(b) Self-activated Specimens

The plain weave architecture provided the best results for the self-activated specimens with roughly 20% healing efficiency. From the results in Table 2 it is also apparent that the virgin toughness for plain weave specimens is slightly decreased once the catalyst is directly embedded into the matrix. The drop in virgin toughness may be associated with the difficulty in manufacturing these specimens. Grubbs' catalyst is a solid at room temperature and it was ground by mortar and pestle until the mean particle size was roughly 28 μm. However, significant clumping of the catalyst particles was unavoidable. Once the catalyst powder was mixed with the matrix resin, some of the clumps were broken up by vigorous stirring, but many large catalyst clusters remained. One cluster of catalyst particles is evident in the lower portion of the image in Fig. 19A.

These clusters lead to a slight decrease in virgin toughness and are a contributing factor to unstable crack propagation (see Fig. 13). Hine *et al.* [14,15] showed that unstable crack growth occurs when a crack moves from one region of high toughness to a region of lower toughness immediately ahead of the crack tip. The stored energy at the moment of propagation is suddenly more than is required for propagation through the region of low toughness and the crack jumps forward. If the catalyst particles can be dispersed uniformly, then the virgin toughness would increase as is demonstrated by particle toughening in other polymeric systems [28,29,30] and in self-activated and self-healing epoxy [1].

11

The high magnification image in Fig. 19B shows a blow-up of the resin rich region surrounding one of the particle clusters. The fracture surface lacks the well defined fiber imprints and fiber breaks characteristic of the fracture surfaces in Figs. 14 and 15. Instead, the surfaces are relatively smooth indicating that the fracture propagated through the resin rich layers surrounding the catalyst particle clusters rather than at the fiber/matrix interface. The spherical objects in Fig. 19B are believed to be polymerized DCPD that was formed in void spaces.

Examination of the fracture surfaces from healed specimens (Fig. 20) again shows evidence of poly(DCPD). The morphology of the polymerized healing agent is quite distinct from the reference specimens (Fig. 17), and many small finger-like patterns are evident on the fracture plane. These fingers under high magnification clearly show that the reason for low healing efficiency (compared to the reference specimens) is incomplete coverage of the fracture plane. In order for the DCPD to polymerize in the self-activated specimen the monomer must come into direct contact with the catalyst, either by touching exposed particles on the fracture plane, or by diffusing a short distance into the matrix and contacting an embedded particle. The polymerization rate in either case is much slower than having mixed the catalyst directly with the healing agent and injecting into the delamination (as with the reference specimens). Evidently the polymerization proceeds so slowly in the embedded catalyst system that a significant amount of the monomer diffuses into the matrix leaving the crack plane dry.

The satin weave specimens exhibited the lowest healing efficiency of any group tested. Their virgin toughness, however, was slightly higher in comparison to the reference specimens (Table 2). Healing efficiency for the satin weave specimens ranged anywhere from 0% (for two specimens) up to about 10%. Since the dominant mode of fracture for these specimens was interfacial failure (see Fig. 15), very little of the catalyst is directly exposed on the fracture plane after virgin testing. Consequently, *in-situ* polymerization of the healing agent was either very slow or nonexistent. The increased healing efficiency for *plain weave* specimens is attributed to the presence of large interstitial areas where Grubbs' catalyst is directly exposed to the fracture plane.

4. General discussion

In light of the fracture test results and microscopic examination of the fracture surfaces there are several controlling factors for healing efficiency that can be identified. For the material system studied in this paper (EPON 828/DETA and E-glass epoxy) the interfacial bond strength between E-glass and the healing agent (DCPD) is critical. Both plain and satin weave specimens failed by interfacial debonding. Thus, the healing agent must bond both to the glass fabric as well as the epoxy matrix in order to achieve

complete repair. The experimental evidence indicates that the interfacial bond strength between poly(DCPD) and E-glass fiber is fairly low. Higher healing efficiencies can be expected by either treating the fiber surface with coupling agents suitable with the healing agent chemistry, or by choosing a more compatible healing agent/fiber system.

To explore the last approach further a series of tests were conducted using two other "healing agents" - epoxy and cyanoacrylate. Plain weave reference specimens were fabricated and injected with EPON 828/DETA after virgin fracture. Results of these tests showed that the average (plateau) healing efficiency was 12%. Satin weave reference specimens were also injected after virgin fracture with cyanoacrylate (Rawn Company, Inc.). The average healing efficiency (plateau) of these specimens was 122%. The results for poly(DCPD) indicate that the interfacial strength for DCPD/E-glass lies somewhere between epoxy and cyanoacrylate.

Unless the healed fracture toughness is nearly equal to the virgin toughness, there is no possibility for fiber bridging to occur in the healed condition. Instead, the crack propagates along the original (virgin) fracture plane where all bridging fibers have already been severed. As such, the R-curve contribution from this important mechanism is sacrificed and the healed toughness will be some fraction of the virgin.

Additionally, the efficiency of healing is directly affected by both the rate of polymerization (*in-situ*) and the degree of polymerization achieved. The slower *in-situ* polymerization rate of the self-activated specimens is believed to have contributed to incomplete coverage of the virgin fracture plane. If the polymerization of the healing agent occurs too slowly then sufficient time is allowed for diffusion of the low molecular weight monomer healing agent into the matrix material (and away from the fracture plane). The result is incomplete coverage of the fracture plane and a lowering of the healing efficiency.

5. Conclusions

A study has been conducted to assess the feasibility of developing a self-healing polymer matrix composite material. Woven glass/epoxy composite DCB specimens were healed by one of two methods. In the first, a catalyzed monomer healing agent (DCPD) was manually injected after fracture. The second approach utilized specimens in which the catalyst was directly embedded in the composite matrix so that the specimen was self-activated once the DCPD monomer was injected.

The results of the DCB testing and microscopic examination of the fracture surfaces revealed three primary factors in determining the level of healing that is achieved in practice. All specimens exhibited interfacial debonding as the dominant mode of failure. Thus, the interfacial bond strength between the healing agent and the

fiber reinforcement is the most critical parameter in selection of the healing agent system. Secondly, the rate of *in-situ* polymerization for self-activated materials must be sufficiently fast so as to prevent diffusion of the monomer into the matrix (thereby leading to incomplete coverage of the healing agent on the fracture plane). Finally, while the role of fiber bridging is important for the inherent toughness of a material, it plays no role in the healed toughness unless the crack path deviates from the original (virgin) fracture plane.

Self-activation of polymerization was demonstrated in E-glass/epoxy plain weave specimens by embedding Grubbs' catalyst (1.75% wt.) into the matrix and injecting DCPD monomer into the fracture plane. The healing efficiency for these specimens was about 20%. Since the healing agent system used in this study produces a living polymerization, repeated healing processes can occur and were demonstrated by successive healing of the same specimen a total of three times.

Finally, the highest healing efficiencies (51-67%) were obtained by specimens in which the monomer was catalyzed manually before injection into the crack plane. Once the rate of *in-situ* polymerization for self-activated specimens is increased (e.g. better dispersion of catalyst particles), then self-activated healing efficiency should be comparable.

Acknowledgements

References

[1] White SR, Sottos NR, Geubelle PH, Moore JS, Kessler MR, Sriram SR, Brown EN, Viswanathan S. Self Healing Composite Materials. Science in review.

[2] Bandyopadhyay S, Gellert EP, Silva VM, Underwood JH. Microscopic Aspects of Failure and Fracture in Cross-Ply Fibre Reinforced Composite Laminates. Journal of Composite Materials 1989;23:1216-1231.

[3] Bascom WD, Bitner JL, Moulton RJ, Siebert AR. The interlaminar fracture of organic-matrix, woven reinforcement composites. Composites 1980;11(1):9-18.

[4] Ebeling, T, Hiltner A, Baer E. Delamination failure of a woven glass fiber composite. Journal of Composite Materials 1997;31(13):1318-1333.

[5] ASTM. Standard test method for mode I interlaminar fracture toughness of unidirectional fiber-reinforced polymer matrix composites. Annual Book of ASTM Standards 1994; D 5528-94a.

[6] Ripling E J, Mostovoy S, Patrick RL. Application of fracture mechanics to adhesive joints. Adhesion, ASTM STP 360, American Society for Testing and Materials, Philadelphia, PA, 1964:5-19.

[7] Bazhenov SL. Strong bending in the DCB interlaminar test of thin, E-glass woven-fabric-reinforced laminates. Composites 1991;22(4):275-280.

[8] Whitney JM, Browning CE, Hoogstenden W. A double cantilever beam test for characterizing mode I delamination of composite materials. Journal of Reinforced Plastics and Composites 1982;1:297-313.

[9] Wang Y, Zhao D. Characterization of interlaminar fracture behaviour of woven fabric reinforced polymeric composites. Composites 1995;26(2):115-124.

[10] Smiley AJ, Pipes RB. *Rate effects on mode I interlaminar fracture toughness in composite materials.* Journal of Composite Materials 1987; 21:670-687.

[11] Hirai Y, Hamada H. Determination of interfacial material constants in plain glass woven fabric using finite element analysis. Composite Interfaces 1997;5(1):69-86.

[12] Kotaki M, and Hamada H. Effect of interfacial properties and weave structure on mode I interlaminar fracture behaviour of glass satin woven fabric composites. Composites - Part A: Applied Science & Manufacturing 1997;28(3):257-266.

[13] Suzuki Y, Maekawa Z, Hamada H, Yokoyama A, Sugihara T, Hojo M. Influence of silane coupling agents on interlaminar fracture in glass fibre fabric reinforced unsaturated polyester laminates. Journal of Materials Science 1993;28(7):1725-1732.

[14] Hine PJ, Brew B, Duckett RA, Ward IM. Fracture behaviour of carbon fibre reinforced poly(ether etherketone). Composites Science and Technology 1988;33:35-71.

[15] Hine PJ, Brew B, Duckett RA, Ward IM. Failure mechanisms in continuous carbon-fibre reinforced PEEK composites. Composites Science and Technology, 1989;35:31-51.

[16] Briscoe BJ, Williams DR. Interlaminar fracture toughness of aramid/epoxy laminates. Composites Science and Technology 1993;46(3):277-286.

[17] Briscoe BJ, Court RS, Williams DR. Effects of fabric weave and surface texture on the interlaminar fracture toughness of aramid/epoxy laminates. Composite Science and Technology 1993;47(3):261-270.

[18] Benzeggagh ML, Gong XJ, Laksimi A, Roelandt JM. On the mode I delamination test and the importance of laminate lay-ups. Polymer Engineering and Science 1991;31(17):1286-1292.

[19] Johnson WS, Mangalgiri PD. Investigation of fiber bridging in double cantilever beam specimens. NASA-TM-87716 1986

[20] Grubbs RH, Chang S. Recent advances in olefin metathesis and its application in organic synthesis. Tetrahedron 1998;54:4413-4450.

[21] ASTM. Standard test method for fiber content of resin-matrix composites by matrix digestion. Annual Book of ASTM Standards 1990; D 3171-76

[22] Hutchinson JW. A Course on Nonlinear Fracture Mechanics 1989: Department of Solid Mechanics, The Technical University of Denmark.

[23] Williams JG. The Fracture Mechanics of Delamination Tests. Journal of Strain Analysis 1989;24(4):207-214.

[24] Ebeling, T, Hiltner A, Baer E. Delamination Failure of a Single Yarn Glass Fiber Composite. Journal of Composite Materials 1997;31(13):1302-1317.

[25] Hwang W, Han KS. Interlaminar fracture behavior and fiber bridging of glass-epoxy composite under mode I static and cyclic loadings. Journal of Composite Materials 1989;23:396-430.

[26] Smith G, Green AK, Bowyer WH. The fracture toughness of glass fabric reinforced polyester resins. In: Stanley P, editor. Fracture Mechanics in Engineering Practice. London: Applied Science Publishers LTD, 1976:271-287.

[27] Jud K, Kausch HH, Williams JG. Fracture mechanics studies of crack healing and welding of polymers. Journal of Material Science 1981;16:204-210.

[28] Lange FF, Radford KC. Fracture energy of an epoxy composite system. Journal of Materials Science 1971;6:1197-1203.

[29] Spanoudakis J, Young RJ. Crack propagation in a glass particle-filled epoxy resin, part 1: Effect of particle volume fraction and size. Journal of Materials Science 1984;19:473-486.

[30] Spanoudakis J, Young RJ. Crack propagation in a glass particle-filled epoxy resin, part 2: Effect of particle-matrix adhesion. Journal of Materials Science 1984;19:487-496.
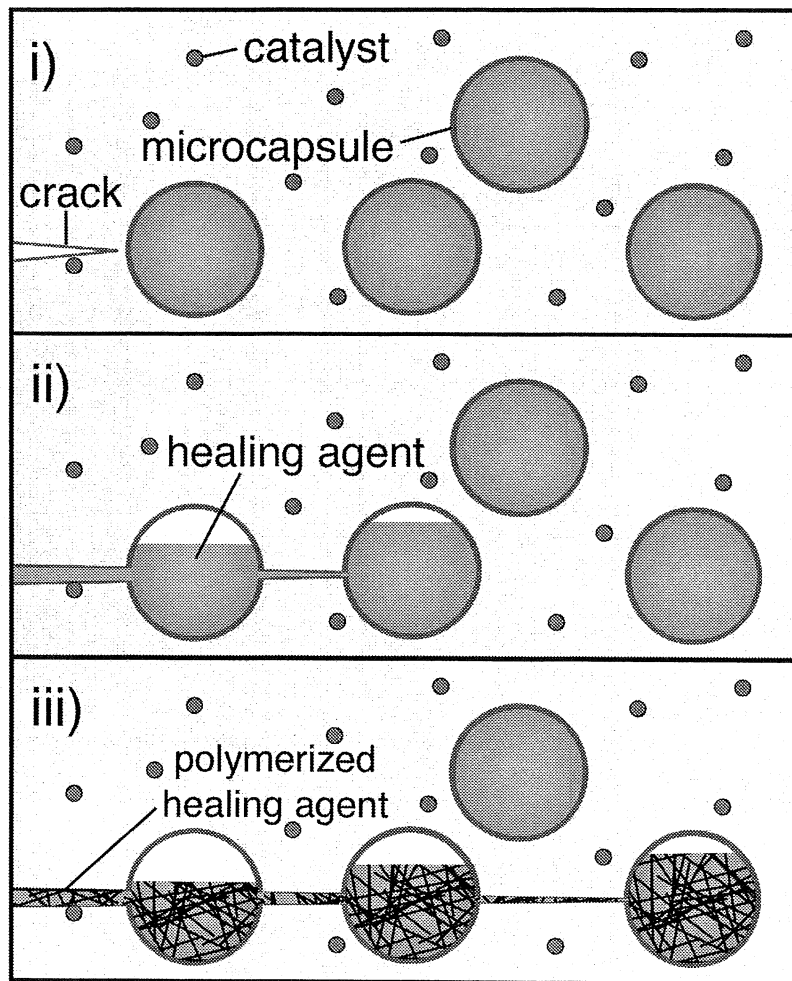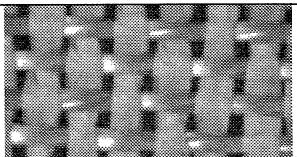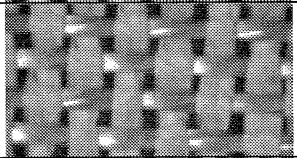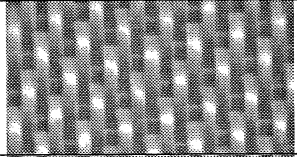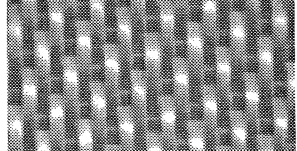
Fig. 1 The self-healing concept. An encapsulated healing agent is embedded into a structural composite matrix containting a catalyst capable of polymerizing the healing agent. i) Cracks form in the matrix wherever damage occurs. ii) The crack ruptures the microcapsules releasing the healing agent into the crack plane through capillary action. iii) The healing agent contacts the catalyst resulting in polymerization that bonds the crack faces closed.

TABLE 1 Types of specmen fabricated for DCB testing

Designation	Catalyst	Fabric	Layers	Spec-imens	Fabric architecture
Reference plain weave	No	E-glass 10 oz/yd^2 0.014" thick 16 x 14 plain weave	10	9	
Self-activated plain weave	Yes*	"	12	10	
Reference satin weave	No	E-glass 9 oz/yd^2 0.008" thick 57 x 54 8H satin	12	6	
Self-activated satin weave	Yes*	"	12	8	

*1.75% mixed with resin used to impregnate center 2 layers of fabric, the equivalent of 0.17 % wt. (satin weave) and 0.33% wt. (plain weave) was also deposited along the midplane in a region extending 75 mm beyond the Teflon insert.
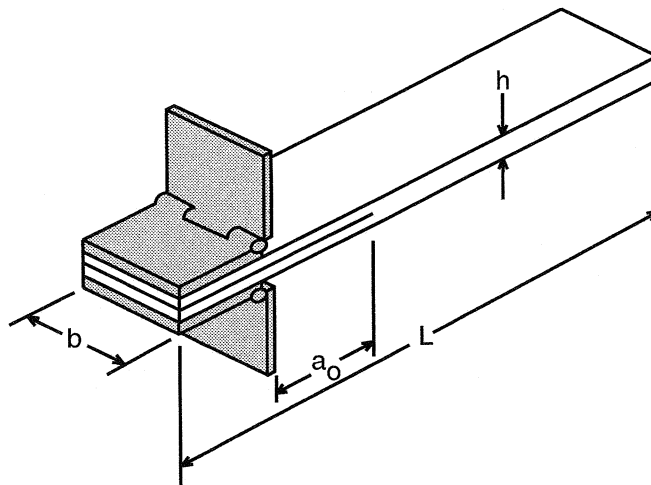
Fig. 2 Double cantilever beam (DCB) specimen.
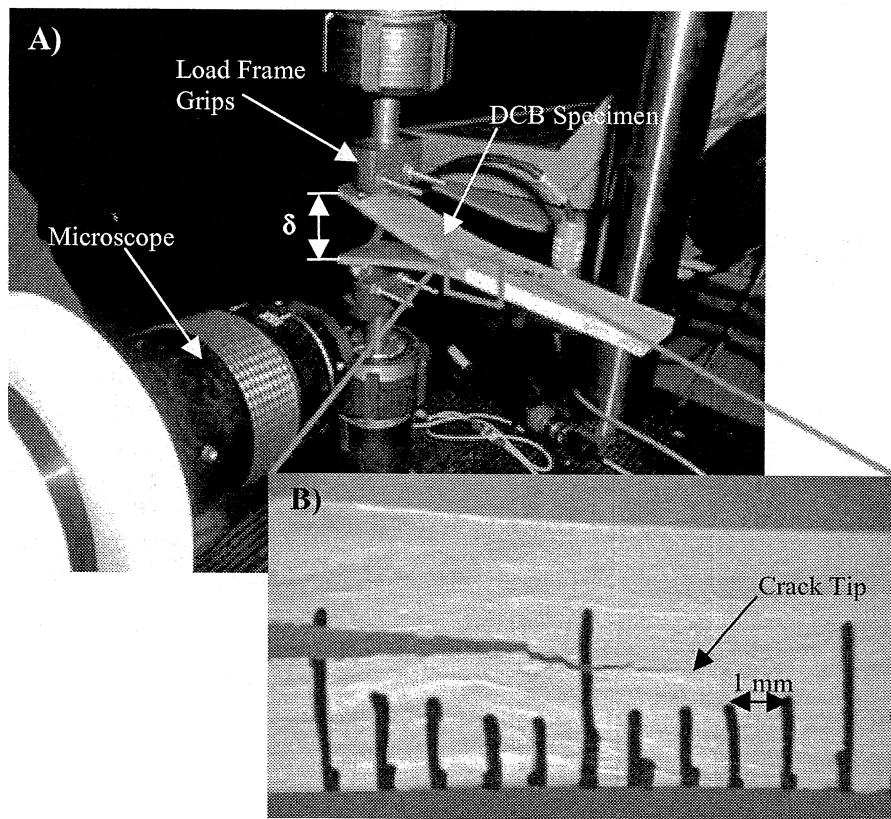
Fig. 3 A) DCB specimen during testing. B) Microscope image of the DCB specimen during testing showing the crack tip position.
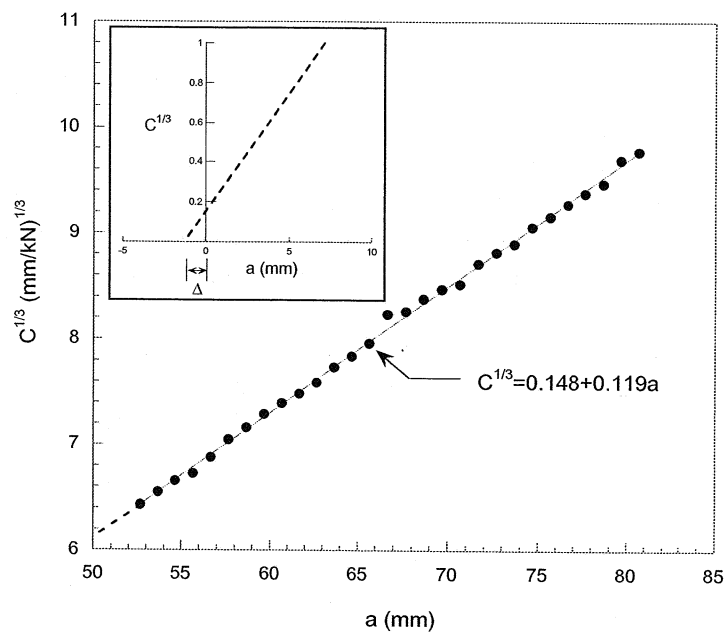

$$C^{1/3} = 0.148 + 0.119a$$

Fig. 4 Cube root of specimen compliance plotted versus crack length to obtain the crack length correction term Δ used in the modified beam theory method.
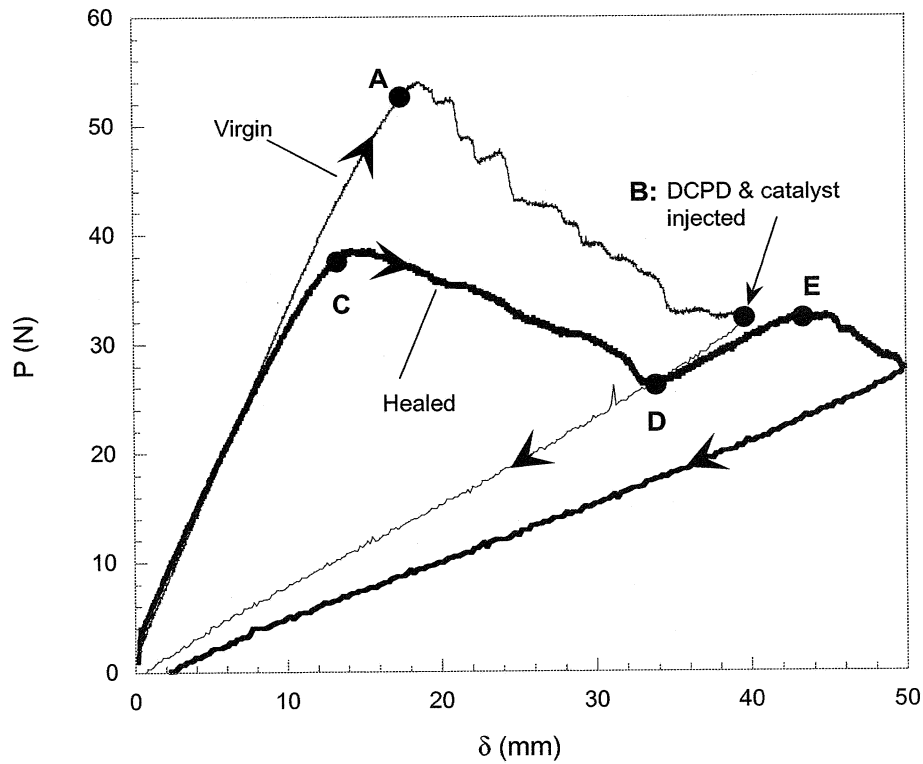
Fig. 5 Typical DCB load-displacement curve for *virgin* and *healed* reference specimens (8H satin weave E-glass/epoxy).

    A. Crack propagation commences for the virgin specimen ahead of the precrack.

    B. Loading of the virgin specimen is completed and a mixture of DCPD monomer and Grubbs' catalyst (1.38% wt.) is injected with a syringe into the delamination. After injection, the specimen is unloaded and the delamination is closed.

    C. Crack propagation commences for the healed specimen.

    D. The crack has propagated through the entire healed region.

    E. Further loading creates a new "virgin" crack ahead of the previously healed region.
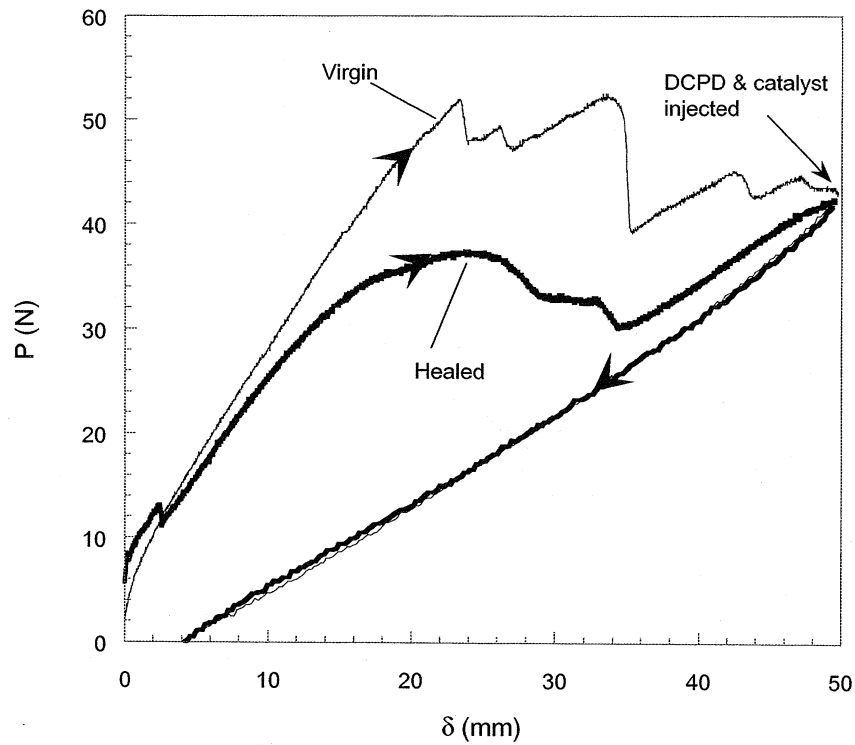
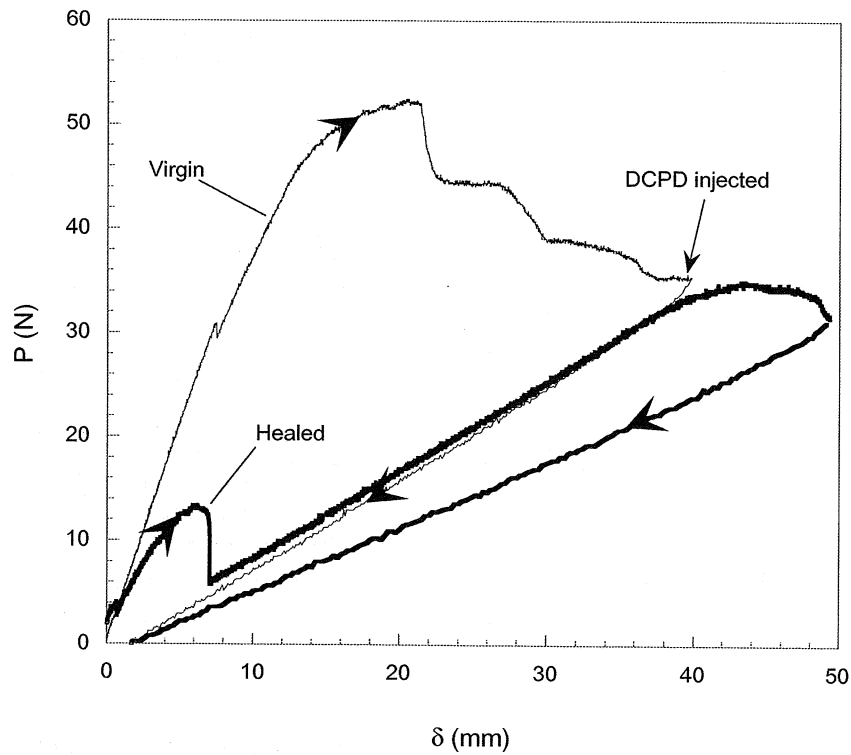Fig. 6 Typical DCB loading curve for virgin and healed reference specimens (plain weave E-glass/epoxy).

Fig. 7 Typical DCB loading curve for virgin and healed self-activated specimens (8H satin weave E-glass/epoxy).
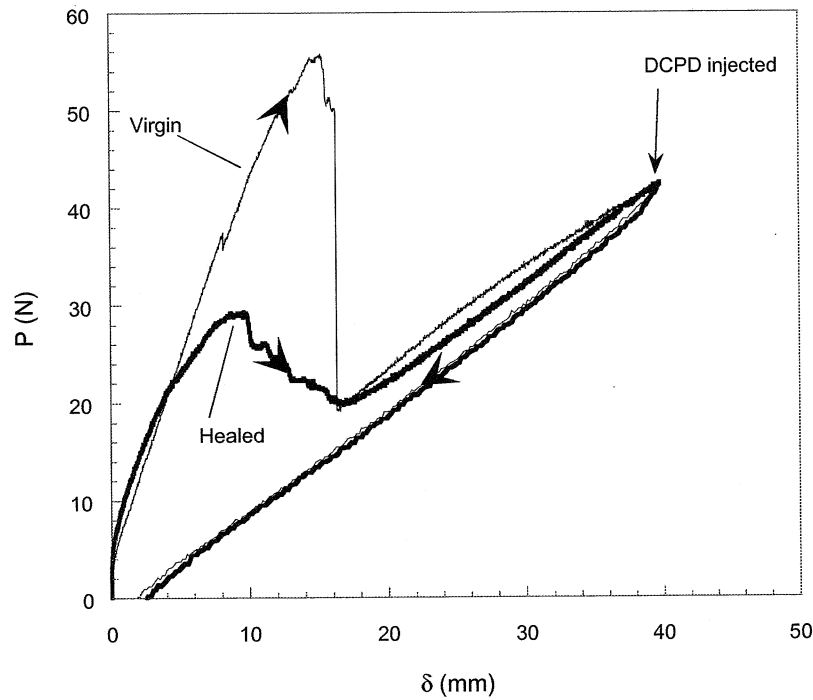
21

Fig. 8 Typical DCB loading curve for virgin and healed self-activated specimens (plain weave E-glass/epoxy).
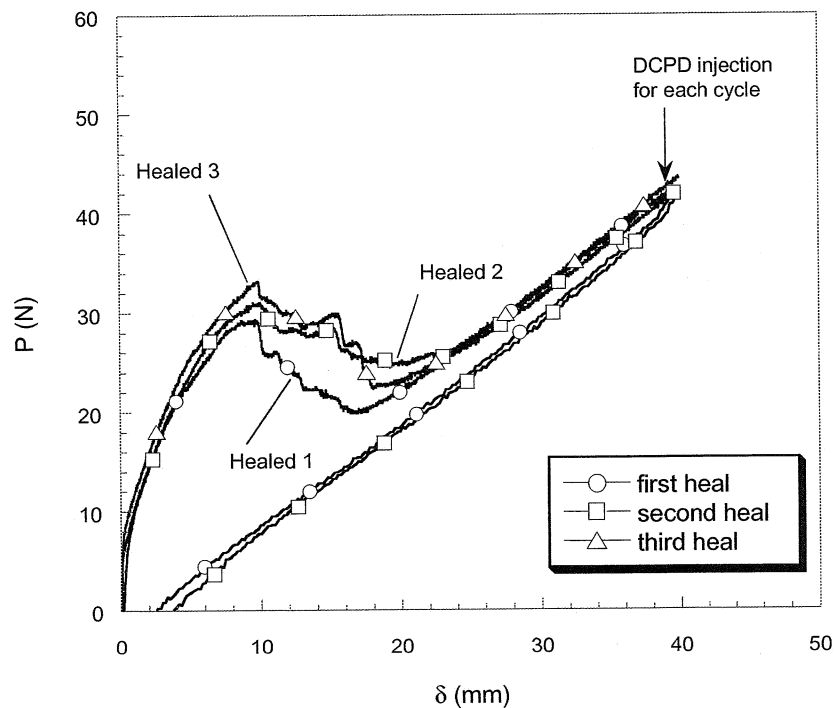

Fig. 9 DCB loading cycles for a self-activated specimen (plain weave E-glass/epoxy) showing multiple healing capability. DCPD monomer is injected after each loading cycle and repeated healing occurs by *living* polymerization of the healing agent-catalyst system.
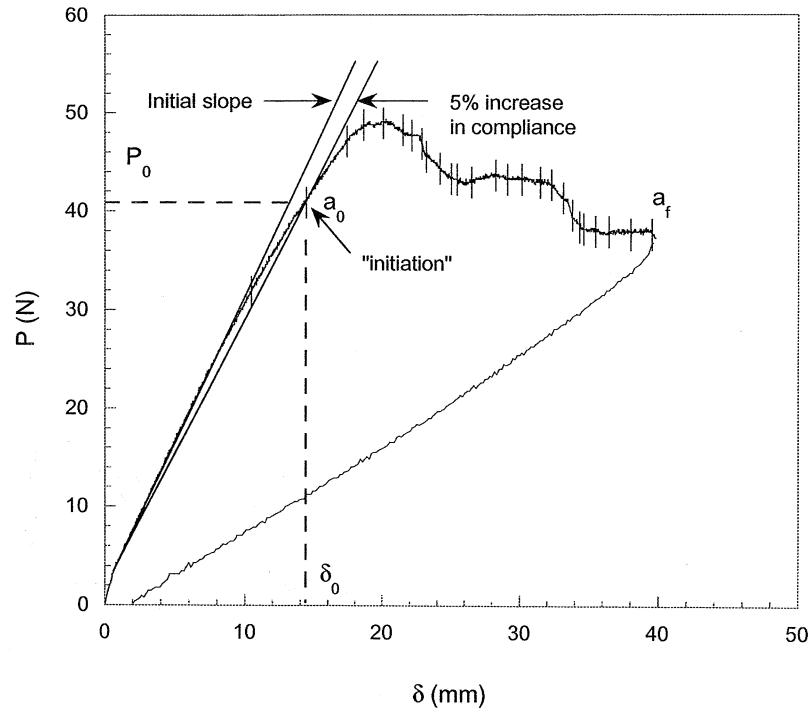
Fig. 10 Data reduction procedure for DCB tests to obtain initiation and subsequent fracture toughness from load-displacement data.
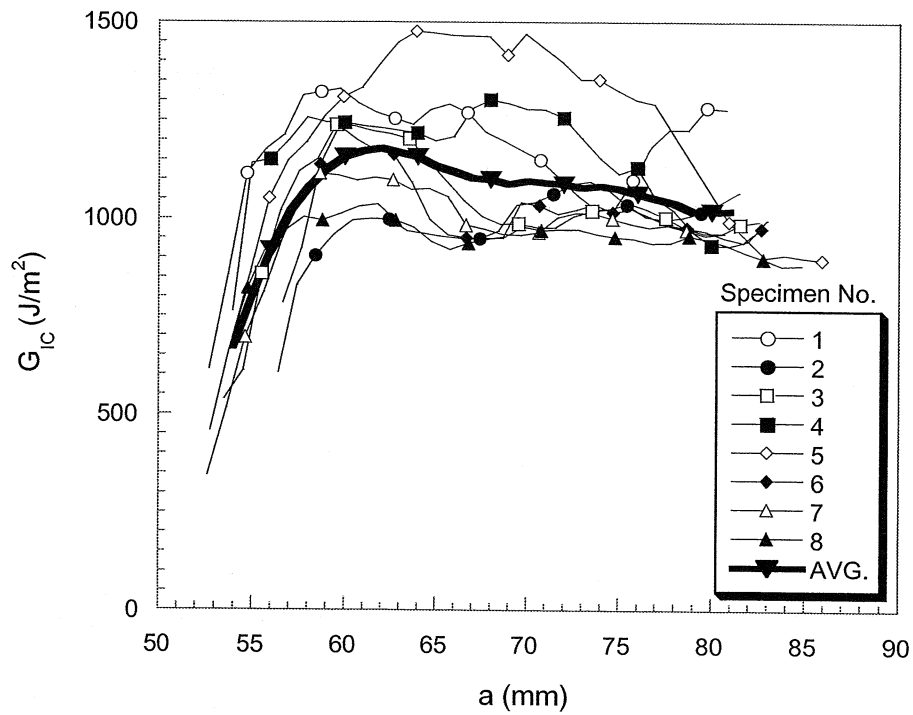

Fig. 11 R-curves for virgin testing of self-activated specimens (8H satin weave E-glass/epoxy).
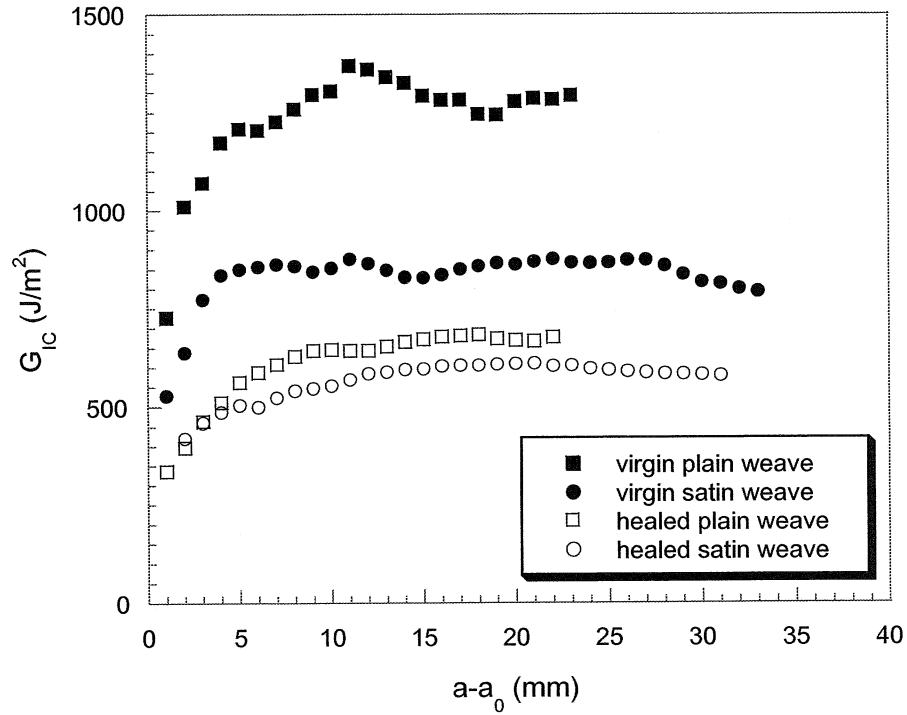
Fig. 12   Average R-curves for the reference specimens.
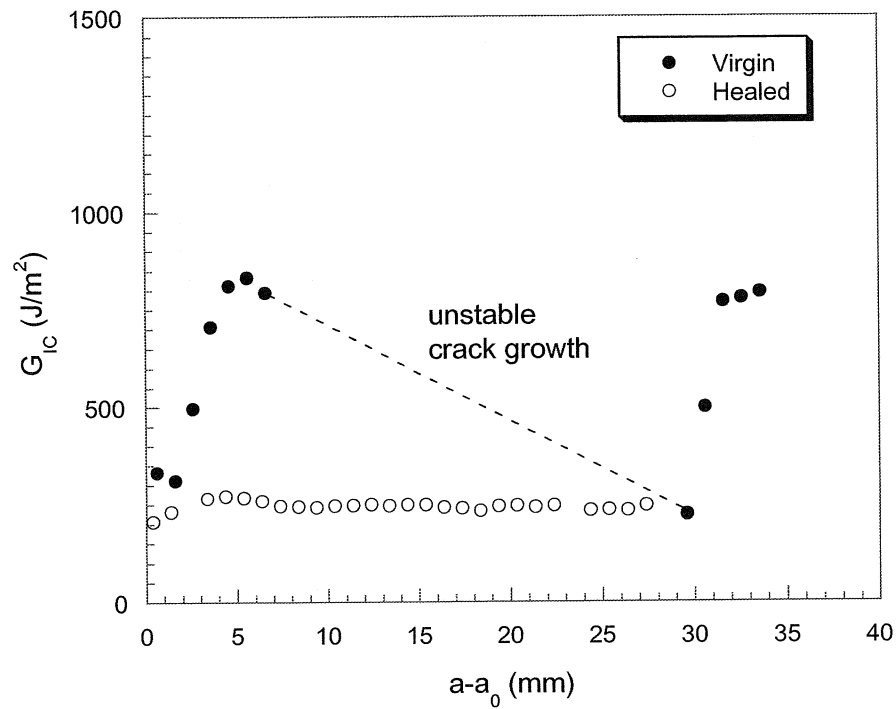

Fig. 13   Typical R-curves for a self-activated plain weave specimen corresponding to the load-displacement curve in Fig. 8. Unstable crack growth in the virgin test is manifest as a sudden drop in fracture toughness when the crack jumps forward.

TABLE 2. Summary of DCB Results

| Specimen		No. of Specimens	G_{IC} virgin Avg. ($\pm$1 S.D.) (J/m^2)		G_{IC} healed Avg. ($\pm$1 S.D.) (J/m^2)		η (%)	
Type	Weave		Initiation	Plateau	Initiation	Plateau	Initiation	Plateau
Reference (standard)	plain	9	726 ($\pm$40)	1283 ($\pm$141)	335 ($\pm$111)	655 ($\pm$223)	46%	51%
	8H satin	6	528 ($\pm$100)	842 ($\pm$171)	420 ($\pm$147)	564 ($\pm$58)	80%	67%
Self-activated (embedded catalyst)	plain	10	644 ($\pm$280)	1052 ($\pm$222)	111 ($\pm$47)	198 ($\pm$57)	17%	19%
	8H satin	8	585 ($\pm$199)	1040 ($\pm$138)	38 ($\pm$56)	87 ($\pm$117)	6.5%	8.4%
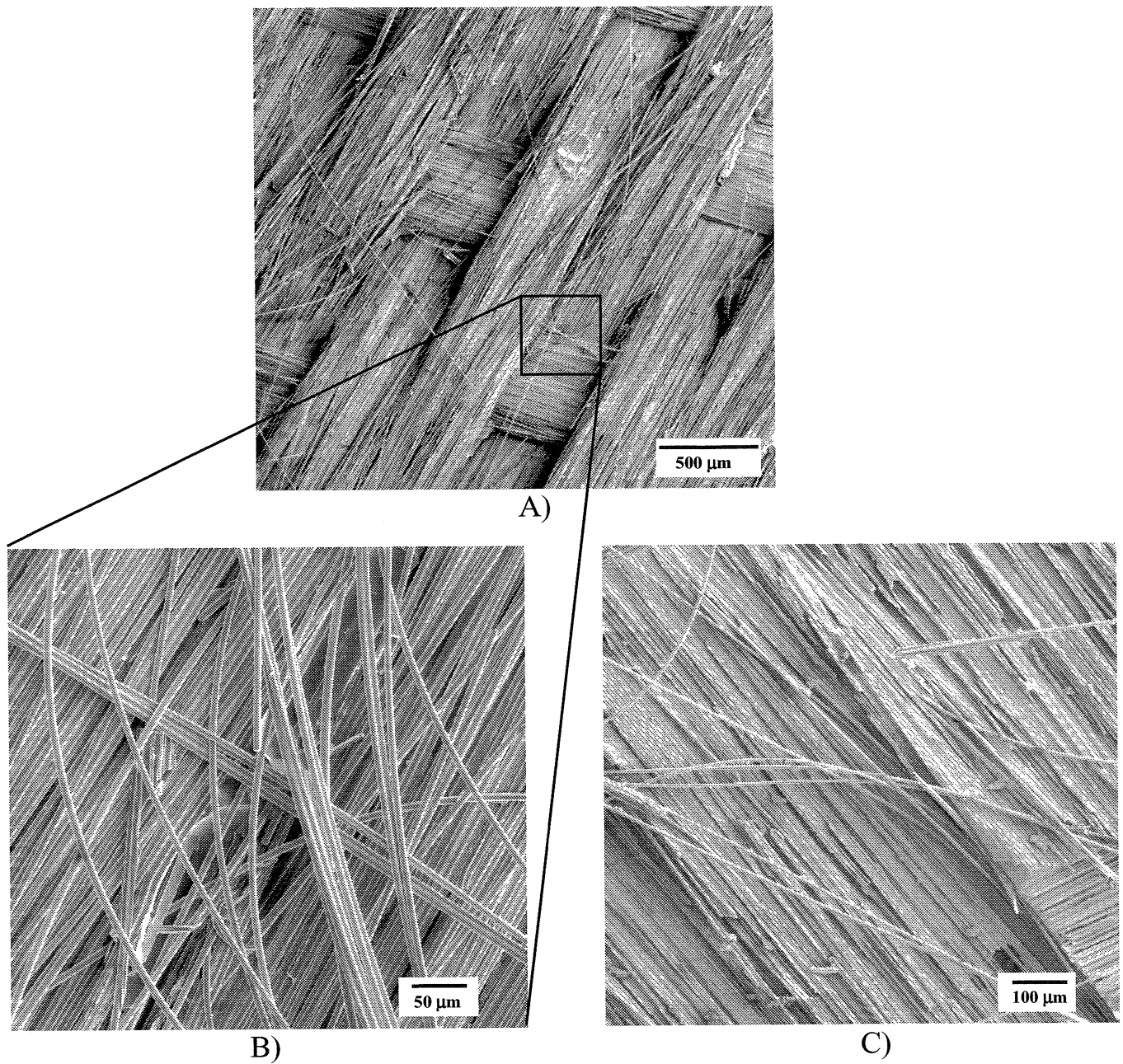
Fig. 14 SEM micrographs of the virgin fracture surface of a satin weave reference specimen.
A) resin lean side of fracture surface
B) high magnification image of (A) showing fiber fracture and debonding
C) high magnification image of resin rich side of fracture surface

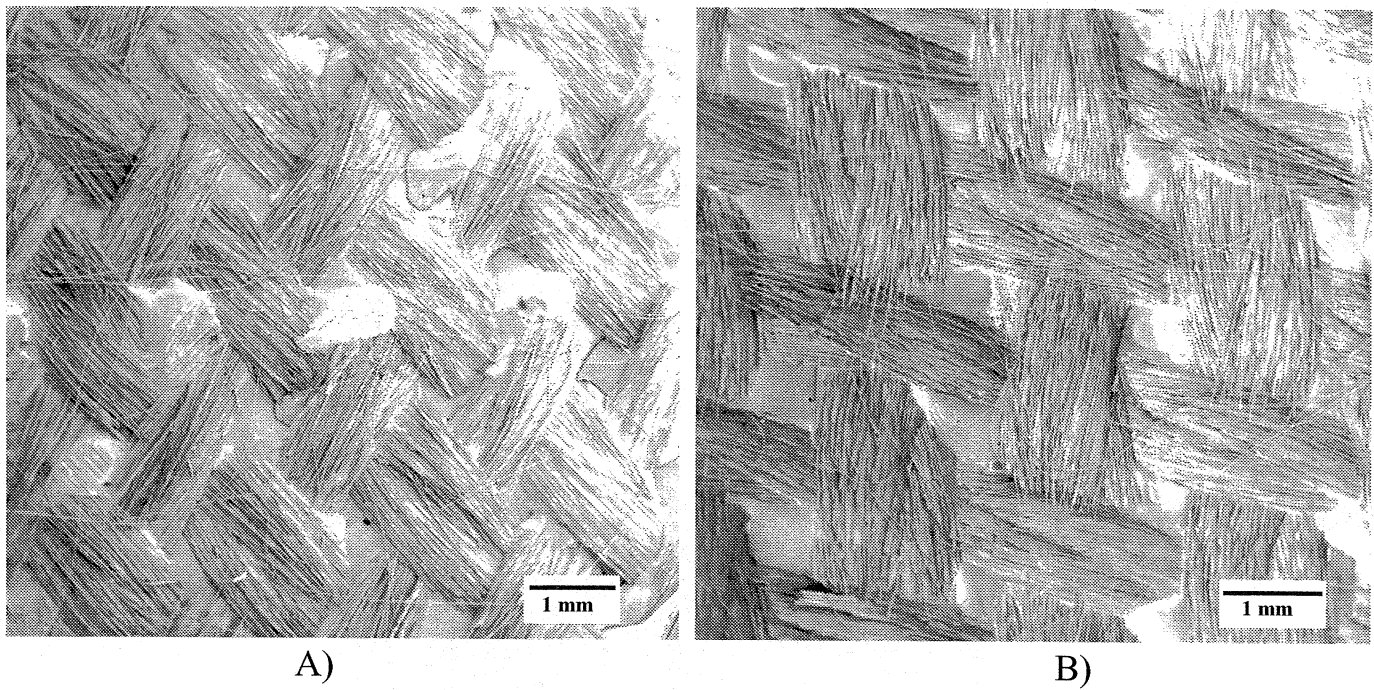A)   B)

Fig. 15 SEM micrographs of the virgin fracture surface of a plain weave reference
specimen.
        A) resin lean side of fracture surface
        B) resin rich side of fracture surface
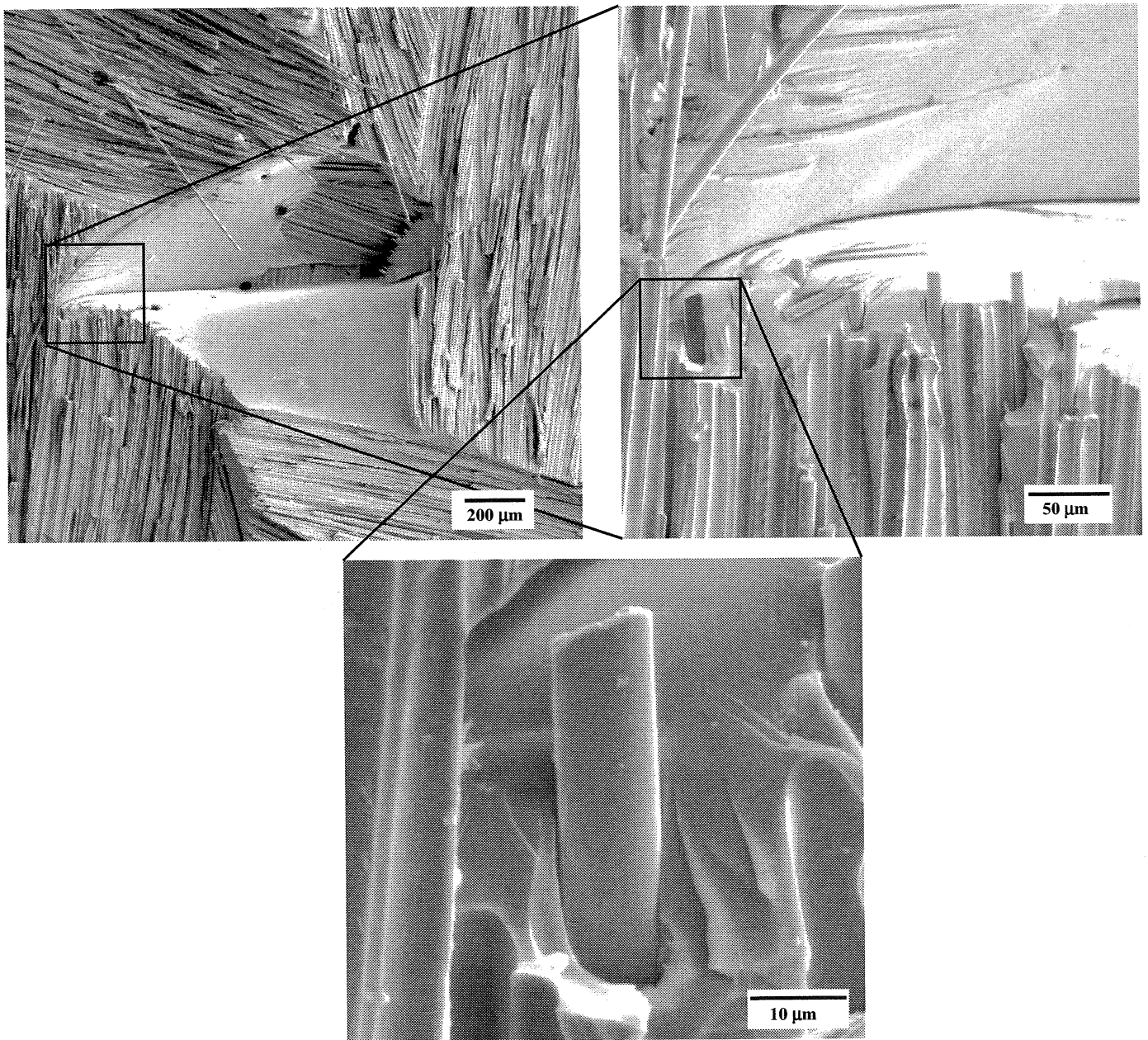
Fig. 16 SEM micrographs at three magnifications of an interstitial area on the virgin fracture surface of a plain weave reference specimen.
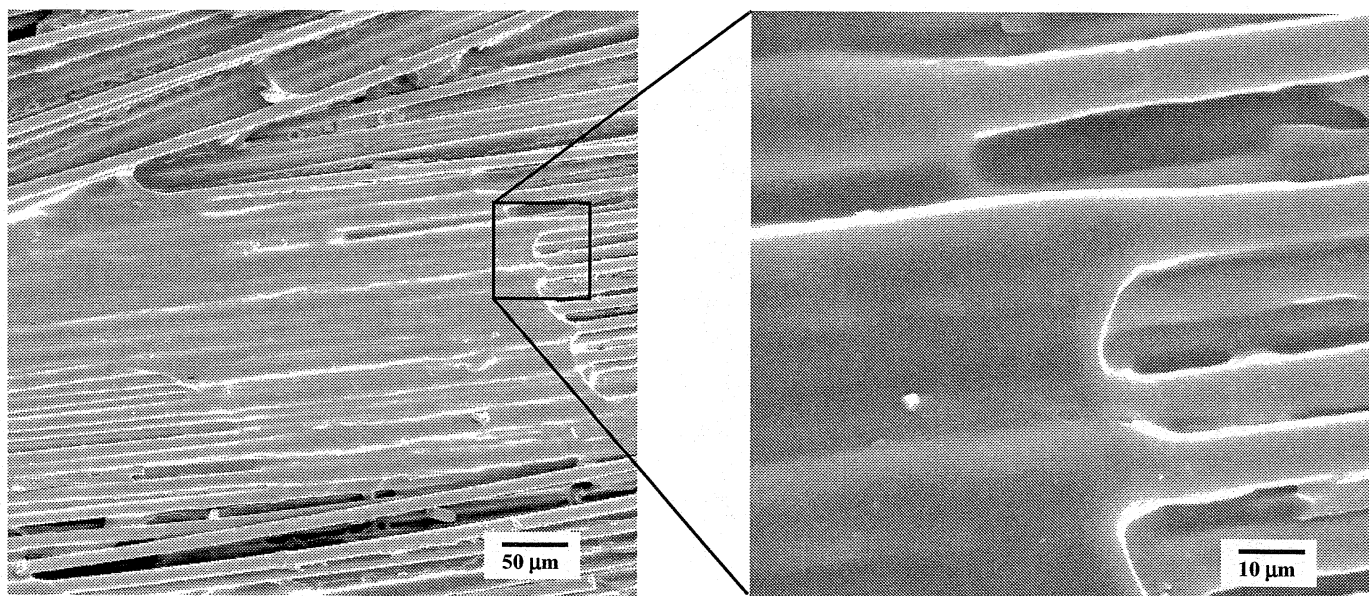
Fig. 17 SEM micrograph of the fracture surface of a healed reference plain weave specimen. The smooth film apparent in the image is polymerized DCPD as confirmed by FTIR analysis.
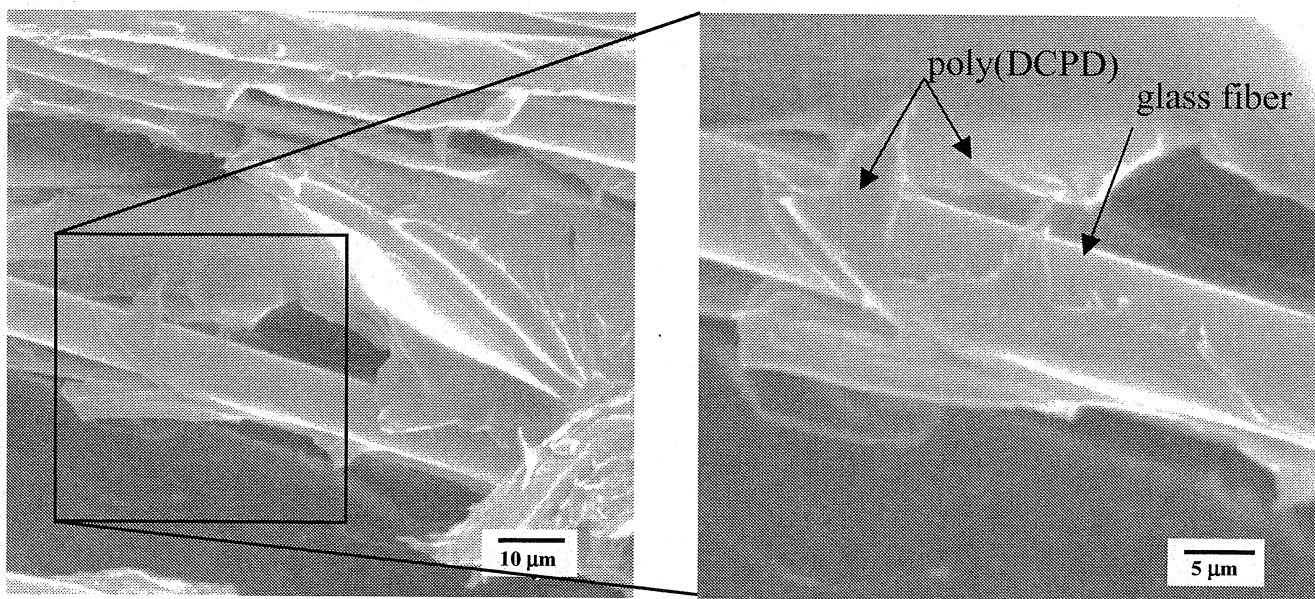
Fig. 18   Close-up view of the polymerized DCPD film on the fracture surface of a healed reference plain weave specimen.

Fig. 19 SEM micrographs of the fracture surface of a typical self-activated plain weave
specimen showing catalyst particle clustering.

Fig. 20 SEM micrographs of the healed fracture plane of a self-activated plain weave
specimen.

List of Recent TAM Reports

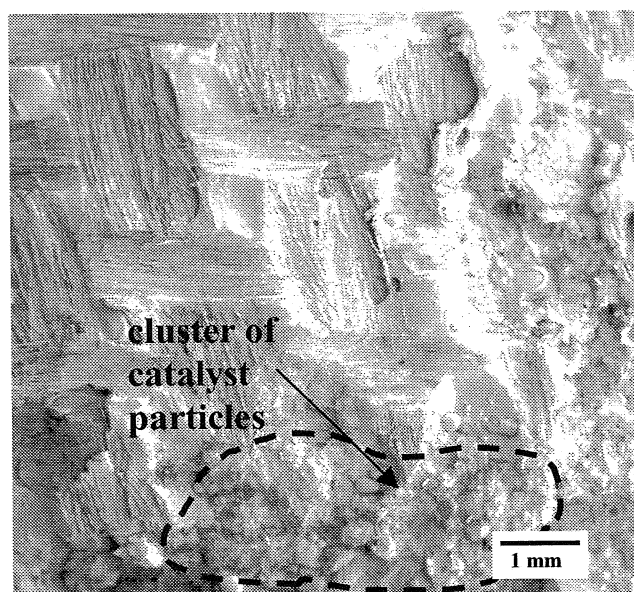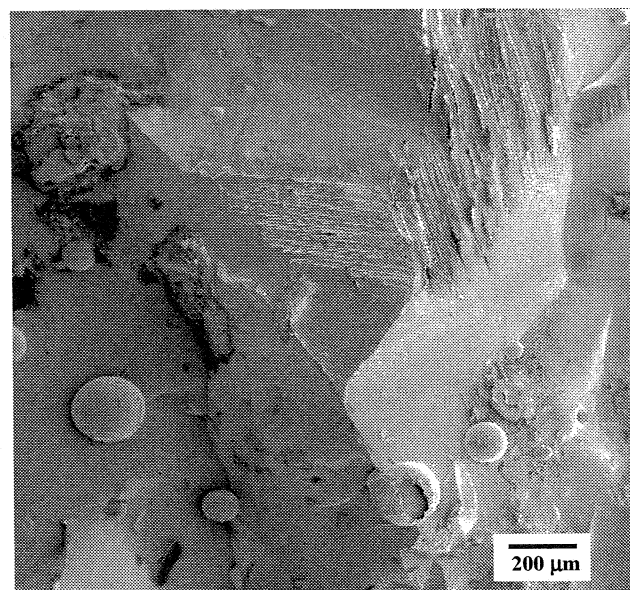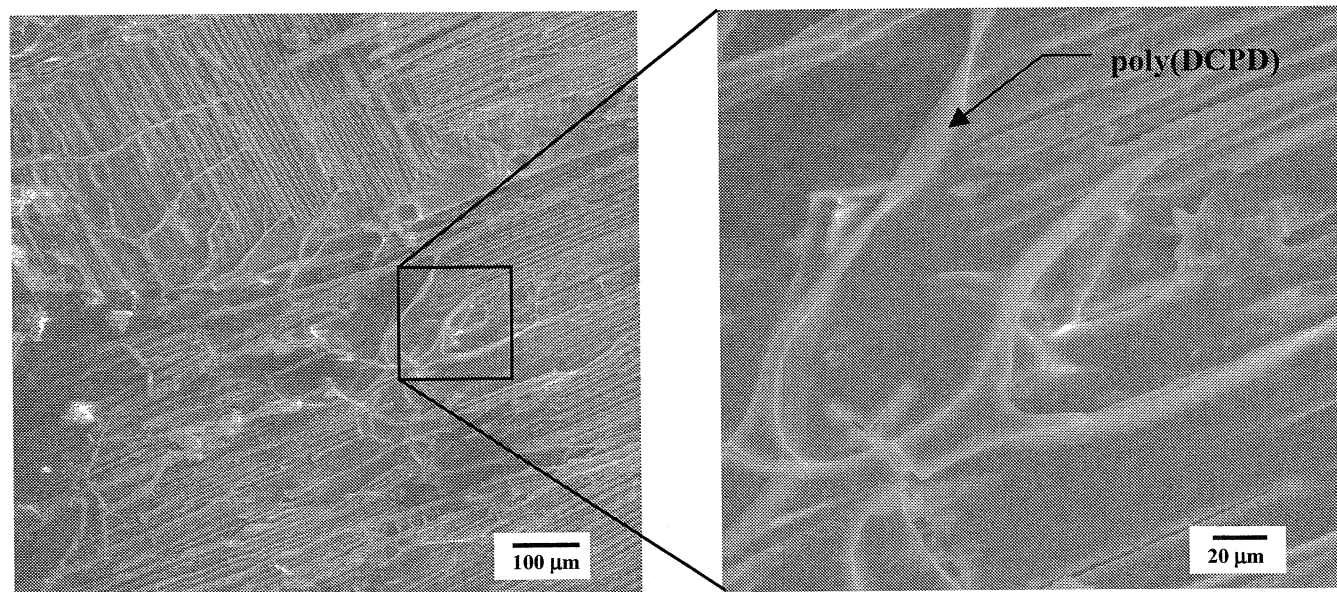| No.	Authors	Title	Date
856	Zhou, Z., R. J. Adrian, S. Balachandar, and T. M. Kendall	Mechanisms for generating coherent packets of hairpin vortices in near-wall turbulence — *Bulletin of the American Physical Society* **42**, 2243 (1997)	June 1997
857	Neishtadt, A. I., D. L. Vainshtein, and A. A. Vasiliev	Chaotic advection in a cubic stokes flow — *Physica D* **111**, 227 (1997).	June 1997
858	Weaver, R. L.	Ultrasonics in an aluminum foam — *Ultrasonics* **36**, 435–442 (1998)	July 1997
859	Riahi, D. N.	High gravity convection in a mushy layer during alloy solidification — In *Nonlinear Instability, Chaos and Turbulence*, D. N. Riahi and L. Debnath, eds., **1**, 301–336 (1998)	July 1997
860	Najjar, F. M., and S. Balachandar	Low-frequency unsteadiness in the wake of a normal plate, *Bulletin of the American Physical Society* **42**, 2212 (1997)	Aug. 1997
861	Short, M.	A parabolic linear evolution equation for cellular detonation instability — *Combustion Theory and Modeling* **1**, 313–346 (1997)	Aug. 1997
862	Short, M., and D. S. Stewart	Cellular detonation stability, I: A normal-mode linear analysis — *Journal of Fluid Mechanics* **368**, 229–262 (1998)	Sept. 1997
863	Carranza, F. L., and R. B. Haber	A numerical study of intergranular fracture and oxygen embrittlement in an elastic–viscoplastic solid — *Journal of the Mechanics and Physics of Solids*, **47**, 27–58 (1997)	Oct. 1997
864	Sakakibara, J., and R. J. Adrian	Whole-field measurement of temperature in water using two-color laser-induced fluorescence — *Experiments in Fluids* **26**, 7–15 (1999)	Oct. 1997
865	Riahi, D. N.	Effect of surface corrugation on convection in a three-dimensional finite box of fluid-saturated porous material — *Theoretical and Computational Fluid Dynamics*, **13**, 189-208 (1999)	Oct. 1997
866	Baker, C. F., and D. N. Riahi	Three-dimensional flow instabilities during alloy solidification — *Bulletin of the American Physical Society* **41**, 1699 (1998)	Oct. 1997
867	Fried, E.	Introduction (only) to *The Physical and Mathematical Foundations of the Continuum Theory of Evolving Phase Interfaces* (book containing 14 seminal papers dedicated to Morton E. Gurtin), Berlin: Springer-Verlag, in press (1998)	Oct. 1997
868	Folguera, A., and J. G. Harris	Coupled Rayleigh surface waves in a slowly varying elastic waveguide — *Proceedings of the Royal Society of London A* **455**, 917–931 (1998)	Oct. 1997
869	Stewart, D. S.	Detonation shock dynamics: Application for precision cutting of metal with detonation waves	Oct. 1997
870	Shrotriya, P., and N. R. Sottos	Creep and relaxation behavior of woven glass/epoxy substrates for multilayer circuit board applications — *Polymer Composites* **19**, 567–578 (1998)	Nov. 1997
871	Riahi, D. N.	Boundary wave–vortex interaction in channel flow at high Reynolds numbers, *Fluid Dynamics Research* **25**, 129–145 (1999)	Nov. 1997
872	George, W. K., L. Castillo, and M. Wosnik	A theory for turbulent pipe and channel flows — paper presented at *Disquisitiones Mechanicae* (Urbana, Ill., October 1996)	Nov. 1997
873	Aslam, T. D., and D. S. Stewart	Detonation shock dynamics and comparisons with direct numerical simulation — *Combustion Theory and Modeling* **3**, 77–101 (1999)	Dec. 1997
874	Short, M., and A. K. Kapila	Blow-up in semilinear parabolic equations with weak diffusion *Combustion Theory and Modeling* **2**, 283-291 (1998)	Dec. 1997
875	Riahi, D. N.	Analysis and modeling for a turbulent convective plume — *Mathematical and Computer Modeling* **28**, 57–63 (1998)	Jan. 1998
876	Stremler, M. A., and H. Aref	Motion of three point vortices in a periodic parallelogram — *Journal of Fluid Mechanics* **392**, 101-128 (1999)	Feb. 1998
877	Dey, N., K. J. Hsia, and D. F. Socie	On the stress dependence of high-temperature static fatigue life of ceramics	Feb. 1998
878	Brown, E. N., and N. R. Sottos	Thermoelastic properties of plain weave composites for multilayer circuit board applications	Feb. 1998

List of Recent TAM Reports (cont'd)

No.	Authors	Title	Date
879	Riahi, D. N.	On the effect of a corrugated boundary on convective motion — *Journal of Theoretical and Applied Mechanics,* in press (1999)	Feb. 1998
880	Riahi, D. N.	On a turbulent boundary layer flow over a moving wavy wall	Mar. 1998
881	Riahi, D. N.	Vortex formation and stability analysis for shear flows over combined spatially and temporally structured walls — *Mathematical Problems in Engineering* **5,** 317–328 (1999)	June 1998
882	Short, M., and D. S. Stewart	The multi-dimensional stability of weak heat release detonations — *Journal of Fluid Mechanics* **382,** 109–135 (1999)	June 1998
883	Fried, E., and M. E. Gurtin	Coherent solid-state phase transitions with atomic diffusion: A thermomechanical treatment — *Journal of Statistical Physics* **95,** 1361–1427 (1999)	June 1998
884	Langford, J. A., and R. D. Moser	Optimal large-eddy simulation formulations for isotropic turbulence — *Journal of Fluid Mechanics* **398,** 321–346 (1999)	July 1998
885	Riahi, D. N.	Boundary-layer theory of magnetohydrodynamic turbulent convection — *Proceedings of the Indian National Academy (Physical Science)* **65A,** 109–116 (1999)	Aug. 1998
886	Riahi, D. N.	Nonlinear thermal instability in spherical shells — in *Nonlinear Instability, Chaos and Turbulence* **2,** 377–402 (1999)	Aug. 1998
887	Riahi, D. N.	Effects of rotation on fully non-axisymmetric chimney convection during alloy solidification — *Journal of Crystal Growth* **204,** 382–394 (1999)	Sept. 1998
888	Fried, E., and S. Sellers	The Debye theory of rotary diffusion	Sept. 1998
889	Short, M., A. K. Kapila, and J. J. Quirk	The hydrodynamic mechanisms of pulsating detonation wave instability — *Proceedings of the Royal Society of London, A* **357,** 3621–3638 (1999)	Sept. 1998
890	Stewart, D. S.	The shock dynamics of multidimensional condensed and gas phase detonations — Proceedings of the 27th International Symposium on Combustion (Boulder, Colo.)	Sept. 1998
891	Kim, K. C., and R. J. Adrian	Very large-scale motion in the outer layer — *Physics of Fluids* **2,** 417–422 (1999)	Oct. 1998
892	Fujisawa, N., and R. J. Adrian	Three-dimensional temperature measurement in turbulent thermal convection by extended range scanning liquid crystal thermometry — *Journal of Visualization* **1,** 355–364 (1999)	Oct. 1998
893	Shen, A. Q., E. Fried, and S. T. Thoroddsen	Is segregation-by-particle-type a generic mechanism underlying finger formation at fronts of flowing granular media? — *Particulate Science and Technology* **17,** 141–148 (1999)	Oct. 1998
894	Shen, A. Q.	Mathematical and analog modeling of lava dome growth	Oct. 1998
895	Buckmaster, J. D., and M. Short	Cellular instabilities, sub-limit structures, and edge-flames in premixed counterflows — *Combustion Theory and Modeling* **3,** 199–214 (1999)	Oct. 1998
896	Harris, J. G.	*Elastic waves* — Part of a book to be published by Cambridge University Press	Dec. 1998
897	Paris, A. J., and G. A. Costello	Cord composite cylindrical shells	Dec. 1998
898	Students in TAM 293–294	Thirty-fourth student symposium on engineering mechanics (May 1997), J. W. Phillips, coordinator: Selected senior projects by M. R. Bracki, A. K. Davis, J. A. (Myers) Hommema, and P. D. Pattillo	Dec. 1998
899	Taha, A., and P. Sofronis	A micromechanics approach to the study of hydrogen transport and embrittlement	Jan. 1999
900	Ferney, B. D., and K. J. Hsia	The influence of multiple slip systems on the brittle–ductile transition in silicon — *Materials Science Engineering A* **272,** 422–430 (1999)	Feb. 1999
901	Fried, E., and A. Q. Shen	Supplemental relations at a phase interface across which the velocity and temperature jump	Mar. 1999

List of Recent TAM Reports (cont'd)

No.	Authors	Title	Date
902	Paris, A. J., and G. A. Costello	Cord composite cylindrical shells: Multiple layers of cords at various angles to the shell axis	Apr. 1999
903	Ferney, B. D., M. R. DeVary, K. J. Hsia, and A. Needleman	Oscillatory crack growth in glass — *Scripta Materialia* **41**, 275–281 (1999)	Apr. 1999
904	Fried, E., and S. Sellers	Microforces and the theory of solute transport	Apr. 1999
905	Balachandar, S., J. D. Buckmaster, and M. Short	The generation of axial vorticity in solid-propellant rocket-motor flows	May 1999
906	Aref, H., and D. L. Vainchtein	The equation of state of a foam	May 1999
907	Subramanian, S. J., and P. Sofronis	Modeling of the interaction between densification mechanisms in powder compaction	May 1999
908	Aref, H., and M. A. Stremler	Four-vortex motion with zero total circulation and impulse — *Physics of Fluids* **11**, 3704-3715	May 1999
909	Adrian, R. J., K. T. Christensen, and Z.-C. Liu	On the analysis and interpretation of turbulent velocity fields — *Experiments in Fluids,* in press (1999)	May 1999
910	Fried, E., and S. Sellers	Theory for atomic diffusion on fixed and deformable crystal lattices	June 1999
911	Sofronis, P., and N. Aravas	Hydrogen induced shear localization of the plastic flow in metals and alloys	June 1999
912	Anderson, D. R., D. E. Carlson, and E. Fried	A continuum-mechanical theory for nematic elastomers	June 1999
913	Riahi, D. N.	High Rayleigh number convection in a rotating melt during alloy solidification — *Recent Developments in Crystal Growth Research,* in press (2000)	July 1999
914	Riahi, D. N.	Buoyancy driven flow in a rotating low Prandtl number melt during alloy solidification — *Current Topics in Crystal Growth Research,* in press (2000)	July 1999
915	Adrian, R. J.	On the physical space equation for large-eddy simulation of inhomogeneous turbulence	July 1999
916	Riahi, D. N.	Wave and vortex generation and interaction in turbulent channel flow between wavy boundaries	July 1999
917	Boyland, P. L., M. A. Stremler, and H. Aref	Topological fluid mechanics of point vortex motions	July 1999
918	Riahi, D. N.	Effects of a vertical magnetic field on chimney convection in a mushy layer — *Journal of Crystal Growth,* in press (2000)	Aug. 1999
919	Riahi, D. N.	Boundary mode–vortex interaction in turbulent channel flow over a non-wavy rough wall	Sept. 1999
920	Block, G. I., J. G. Harris, and T. Hayat	Measurement models for ultrasonic nondestructive evaluation	Sept. 1999
921	Zhang, S., and K. J. Hsia	Modeling the fracture of a sandwich structure due to cavitation in a ductile adhesive layer	Sept. 1999
922	Nimmagadda, P. B. R., and P. Sofronis	Leading order asymptotics at sharp fiber corners in creeping-matrix composite materials	Oct. 1999
923	Yoo, S., and D. N. Riahi	Effects of a moving wavy boundary on channel flow instabilities	Nov. 1999
924	Adrian, R. J., C. D. Meinhart, and C. D. Tomkins	Vortex organization in the outer region of the turbulent boundary layer	Nov. 1999

No.	Authors	Title	Date
925	Riahi, D. N., and A. T. Hsui	Finite amplitude thermal convection with variable gravity — *International Journal of Mathematics and Mathematical Sciences,* in press (2000)	Dec. 1999
926	Kwok, W. Y., R. D. Moser, and J. Jiménez	A critical evaluation of the resolution properties of *B*-spline and compact finite difference methods	Feb. 2000
927	Ferry, J. P., and S. Balachandar	A fast Eulerian method for two-phase flow	Feb. 2000
928	Thoroddsen, S. T., and K. Takehara	The coalescence–cascade of a drop	Feb. 2000
929	Liu, Z.-C., R. J. Adrian, and T. J. Hanratty	Large-scale modes of turbulent channel flow: Transport and structure	Feb. 2000
930	Borodai, S. G., and R. D. Moser	The numerical decomposition of turbulent fluctuations in a compressible boundary layer	Mar. 2000
931	Balachandar, S., and F. M. Najjar	Optimal two-dimensional models for wake flows	Mar. 2000
932	Yoon, H. S., K. V. Sharp, D. F. Hill, R. J. Adrian, S. Balachandar, M. Y. Ha, and K. Kar	Integrated experimental and computational approach to simulation of flow in a stirred tank	Mar. 2000
933	Sakakibara, J., Hishida, K., and W. R. C. Phillips	On the vortical structure in a plane impinging jet	Apr. 2000
934	Phillips, W. R. C.	Eulerian space–time correlations in turbulent shear flows	Apr. 2000
935	Hsui, A. T., and D. N. Riahi	Onset of thermal–chemical convection with crystallization within a binary fluid and its geological implications	Apr. 2000
936	Cermelli, P., E. Fried, and S. Sellers	Configurational stress, yield, and flow in rate-independent plasticity	Apr. 2000
937	Adrian, R. J., C. Meneveau, R. D. Moser, and J. J. Riley	Final report on 'Turbulence Measurements for Large-Eddy Simulation' workshop	Apr. 2000
938	Bagchi, P., and S. Balachandar	Linearly varying ambient flow past a sphere at finite Reynolds number — Part 1: Wake structure and forces in steady straining flow	Apr. 2000
939	Gioia, G., A. DeSimone, M. Ortiz, and A. M. Cuitiño	Folding energetics in thin-film diaphragms	Apr. 2000
940	Chaïeb, S., and G. H. McKinley	Mixing immiscible fluids: Drainage induced cusp formation	May 2000
941	Thoroddsen, S. T., and A. Q. Shen	Granular jets	May 2000
942	Riahi, D. N.	Non-axisymmetric chimney convection in a mushy layer under a high-gravity environment	May 2000
943	Christensen, K. T., S. M. Soloff, and R. J. Adrian	PIV Sleuth: Integrated particle image velocimetry interrogation/validation software	May 2000
944	Wang, J., N. R. Sottos, and R. L. Weaver	Laser induced thin film spallation	May 2000
945	Riahi, D. N.	Magnetohydrodynamic effects in high gravity convection during alloy solidification	June 2000
946	Gioia, G., Y. Wang, and A. M. Cuitiño	The energetics of heterogeneous deformation in open-cell solid foams	June 2000
947	Kessler, M. R., and S. R. White	Self-activated healing of delamination damage in woven composites	June 2000